Technical Report 1609
May 1993

Ocean Surface Roughness from Infrared Measurements: A Failure of Shape from Reflection

K. D. Anderson

NRaD

Technical Report 1609
May 1993

Ocean Surface Roughness from Infrared Measurements: A Failure of Shape from Reflection

K. D. Anderson

NAVAL COMMAND, CONTROL AND OCEAN SURVEILLANCE CENTER
RDT&E DIVISION
San Diego, California 92152–5001

K. E. EVANS, CAPT, USN
Commanding Officer

R. T. SHEARER
Executive Director

ADMINISTRATIVE INFORMATION

This work was performed by the Tropospheric Branch of the Ocean and Atmospheric Sciences Division and was sponsored by the Major Bid & Proposal (MB&P) program of the Naval Command, Control and Ocean Surveillance Center, RDT&E Division.

Released by
R. A. Paulus, Head
Tropospheric Branch

Under authority of
J. H. Richter, Head
Ocean and Atmospheric
Sciences Division

RV

EXECUTIVE SUMMARY

OBJECTIVE

This report describes an approach taken to test the practicality of an instrument that uses the reflection coefficient modulated radiance (shape from reflection) to measure the roughness of the ocean surface. Conceptually, this instrument would be used remotely aboard ship to sense the ocean wave spectrum of the ocean surface; ideally, the ocean wave spectrum covered by this instrument would range from very long wavelengths, on the order of decameters, to very short wavelengths, on the order of centimeters.

RESULTS

A series of wave-tank measurements made at the Scripps Institution of Oceanography (SIO), San Diego, CA, clearly show that the technique of using the reflection coefficient modulated radiance to measure surface roughness is impractical. The technical difficulties are associated with the failure of several necessary assumptions of shape from reflection. The first assumption is that the "sky" illumination source is nearly isotropic; in practice, this assumption is not valid. The second assumption is that the nonlinear relationship between the reflection coefficient and wave slope is not a fundamental limiting factor; in practice, the sensitivity of the reflection coefficient to incidence angle appears to be a limiting factor.

RECOMMENDATIONS

It is recommended that the technique of shape from reflection be abandoned as a method to assess the ocean surface roughness.

CONTENTS

ILLUSTRATIONS

ILLUSTRATIONS (continued)

TABLES

INTRODUCTION

The sea surface is of fundamental importance to U.S. Navy operations not only because it is the milieu of the surface fleet, but also because it significantly contributes to radar clutter, acoustic and electromagnetic signal propagation, and boundary layer interactions. Heavy seas, caused by a hurricane or a typhoon, may extensively modify fleet deployment plans. A moderately rough surface may increase the ambient acoustic noise level, thereby reducing the maximum detection range of underwater targets. Above the surface, a rough sea may reduce a radar system's detection range by decreasing the magnitude of the reflection coefficient.

Statistical measures of the sea surface are regarded in ocean wave analysis as the only descriptors that are significant, both observationally and theoretically, because the surface shape varies in an irregular and unpredictable manner in both space and time. These statistical measures vary in complexity from visual estimates of the significant wave height to measurements of the energy spectra, either of the surface function (the displacement of the surface from some reference height), or of the wave slope. The distinctions between the statistical measures are related to the wavelengths-of-interest and to the instruments used in the measurements. Long wavelengths, on the order of decameters and greater, affect ship maneuverability and are associated with surface displacements that can be measured by satellite-borne radars. Moderate wavelengths, on the order of meters and greater, affect acoustic signal propagation and can be measured by instruments such as buoy-mounted accelerometers and resistive wire gauges (wave staffs). Short wavelengths, on the order of centimeters and less, affect electromagnetic signal propagation and are associated with small surface displacements and large slopes that can only be measured using noncontact electro-optic techniques.

High sea states are associated with long wavelengths and are generally easy to predict because these conditions are associated with large-scale forcing functions (hurricanes or typhoons) that are themselves easy to detect and track. The time and length scales of the driving forces are synoptic; that is, lengths are on the order of 100 km and greater, with time scales on the order of days to weeks. Wind-generated, short wavelength, small-gravity and capillary waves are created by localized meteorologic and oceanic conditions that are difficult to predict without in situ measurements. The scales of short wavelength driving forces are on the order of a kilometer or less, with time scales on the order of seconds to minutes (microscale). Moderate wavelength seas result from a combination of synoptic scale, mesoscale (1 to 100 km, minutes to days), and microscale atmospheric and oceanic conditions.

Onboard Tactical Decision Aids (TDAs) have been developed to assist operational forces in exploiting or mitigating environmental effects. Ship response TDAs can be used to assess maneuverability in various sea states. Acoustic and electromagnetic TDAs assist in determining maximum sensor detection ranges against selected targets. Although computerized tools exist to assess the effect of surface roughness, it is rarely measured directly, but is usually inferred from observations of wind speed, or from estimates of the significant wave height. In most cases, the inferred information is adequate for TDAs because they were developed with the knowledge that only secondary information (e.g., wind speed) would be available on a routine basis. If additional information, such as the wave spectrum, were to become readily available, most of the TDAs could be updated to include a wave spectrum description of surface roughness, perhaps substantially improving the prediction.

Although a number of instruments exist to measure the spectra of wind-generated, small-gravity, capillary waves in laboratory, or near-laboratory conditions, currently, none are available for use aboard operational ships. Instruments to measure the moderate wavelength spectra are also not applicable for use aboard operational ships. A field of buoys could be deployed within a day (at best), but is generally considered impractical because of the expense, and because the buoy field would be essentially stationary. Resistive wire gauges are too delicate for shipboard use, and they require periodic calibrations and cleaning.

The advantages of an onboard, in situ, wave spectra measurement instrument extend beyond possible improvements in TDA prediction capabilities. The improvements in basic research could be considerable; for example, such an instrument would be valuable to both acoustic and electromagnetic propagation measurement programs to firmly establish the underlying relationships of surface roughness to propagation. Routine surface spectral measurements would benefit both global climatology and pollution studies.

The concept of such an instrument is straight forward. A detector (figure 1) looks down on the surface of the water and measures the radiance emitted and reflected from the surface. The measured radiance L (in two dimensions and neglecting any path transmittance effects) is

$$L = (1/\pi) \iint [\beta_s(1 - \varrho) + \varepsilon_a \beta_a \varrho] \, d\lambda \, d\theta \qquad (1)$$

where β_s is the black-body radiant emittance of the surface; ϱ is the Fresnel reflection coefficient evaluated at the reflection angle Ω; ε_a is the emissivity of the air source; β_a is the black-body radiant emittance of the air source; λ is the wavelength of the radiation, and θ is the depression angle between the detector and the surface element. The $1/\pi$ term is needed for Lambertian surfaces. If β_s and $\varepsilon_a \beta_a$ are approximately constant over λ and θ, then the measured radiance L is modulated by ϱ. By selecting λ, ϱ becomes a strong function of Ω, which is itself a strong function of the surface slope angle α; therefore, the radiance can be strongly connected to the slope of the wave. If the spectrum of the wave slope is known, then the spectrum of the surface function ς is also known.

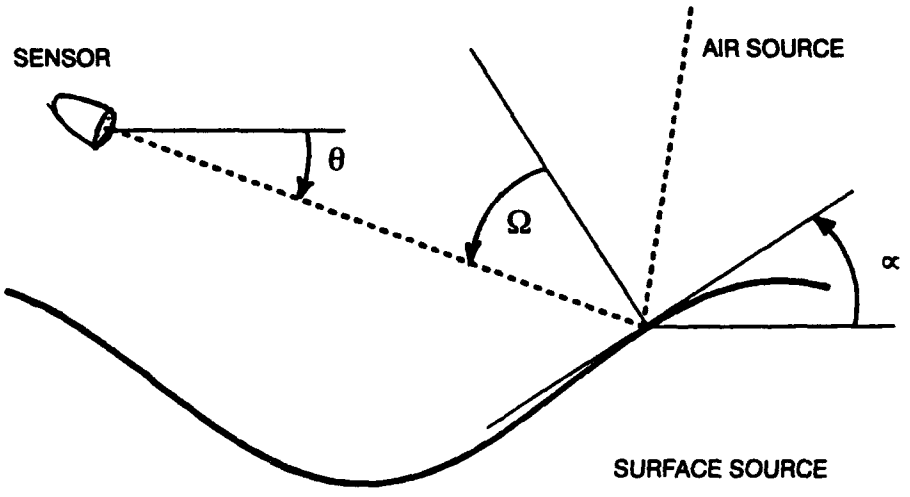

Figure 1. The geometry of an instrument to measure the ocean surface height.

The following section describes an approach taken to test the practicality of an instrument that uses the reflection coefficient modulated radiance to measure surface roughness. After a review of the physics and sensor characteristics, results from a series of wave-tank measurements are examined. It is concluded that the technique is not adequate to measure the moderate- and short-wavelength spectrum. The nonlinear nature of the ϱ-α relationship and the assumption of a constant sky radiator are the major sources of error. Even though the technique is not satisfactory, the methods and results are documented not only to prevent future studies from pursuing this path, but to encourage and challenge other investigator's to examine new techniques of remotely sensing the ocean surface roughness from in situ measurements.

SHAPE FROM REFLECTION

The technique to determine the surface roughness from the reflection coefficient modulated radiance is referred to as "shape from reflection," (Jahne, Waas, and Klinke, 1992). Stilwell (1969) was the first to propose using photographic techniques to determine the surface spectra by shape from reflection. His method is known as Stilwell photography. The critical assumptions are an isotropic (or nearly isotropic) skylight luminance and a uniform surface temperature. Then, the radiance depends only on the reflection coefficient.

Radiant emittance β_λ (mW cm^{-2} μm^{-1}) is related to black-body temperature and the wavelength of the radiation through the Planck equation;

$$\beta_\lambda = 2\ \pi\ c^2 h/[10\lambda^5(e^{hc/\lambda k_b T} - 1)] \qquad (2)$$

where c is the speed of light; h is Planck's constant: k_b is Boltzman's constant, and T is the temperature (Kelvin).

A Lambertian surface is a perfectly diffuse surface that has a constant radiance independent of viewing direction. The constant radiance is the radiant emittance per unit solid angle

$$L_\lambda = \beta_\lambda/\pi \qquad (3)$$

which is expressed in units of mW cm^{-1} sr^{-2} μm^{-1}.

The sensing system was chosen to operate in the far infrared for several reasons: first, in the 8- to 12-micron (μm) band, the small optical depth of water reduces the effects of internal scatter (radiation penetrating the surface and scattering back out at some other angle); second, unlike some methods that rely on the sun as a source of photons, the sensors would be able to operate day and night (but with fewer available photons); third, sensors operating in the 8- to 12-μm band were available for use. These sensors were Everest Interscience Inc., Model 4000, that had been purchased to support other experimental efforts. The field-of-view (fov) angle for these sensors is 4 degrees.

Figure 2 shows the black-body temperature with respect to the band averaged 8- to 12-μm radiance L. The T-L relation is slightly nonlinear over the entire temperature range shown, from 0 to 40 degrees; however, over smaller temperature segments (of about 10 degrees), the T-L relation is nearly linear.

In the infrared, the refractive index of water η is well known (Hale and Querry, 1973). Figure 3 shows the relationship between the complex refractive index of saline water and wavelength (values

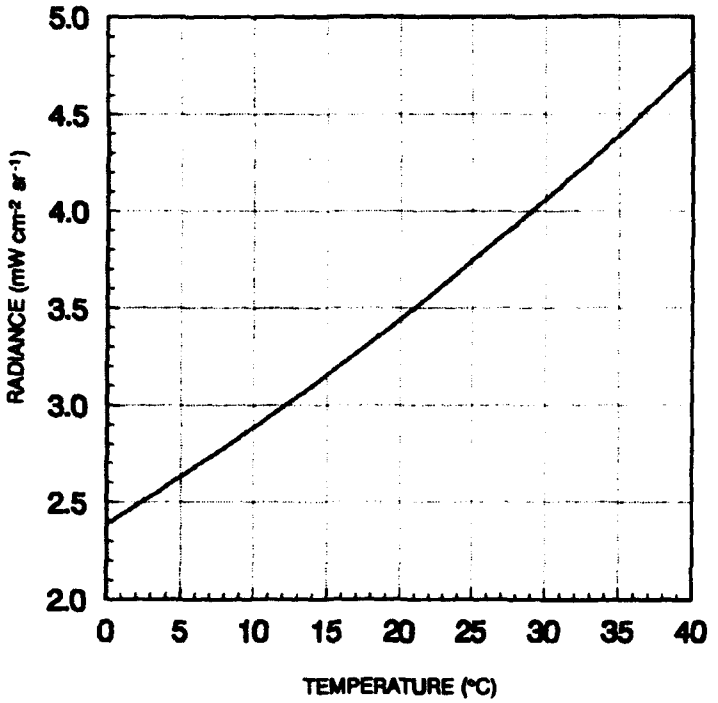

Figure 2. Band average black-body radiance in relation to the black-body temperature.

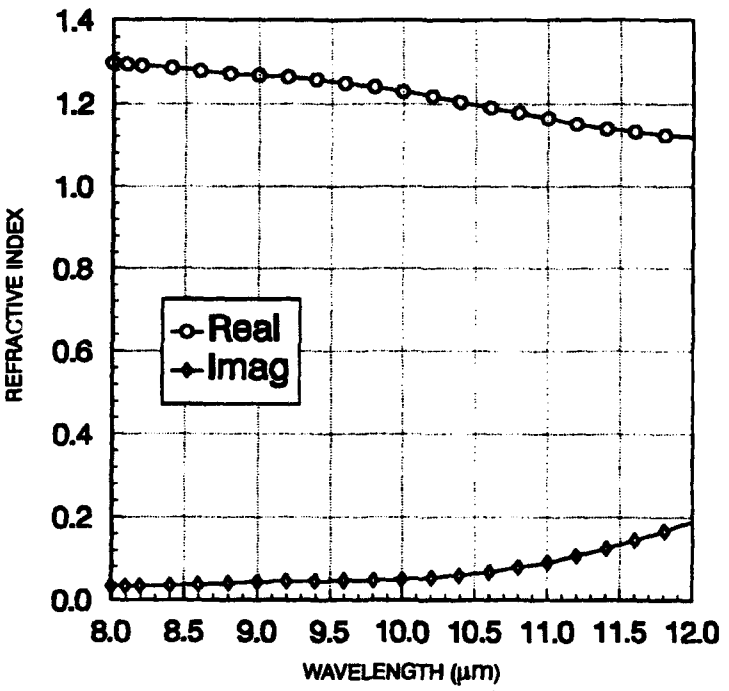

Figure 3. The refractive index of saline water. The values correspond to water taken from the Pacific Ocean (Querry et al., 1977).

from Querry et al., 1977, table 3, Pacific Ocean); the circles represent the real part of η, and the diamonds represent the imaginary part of η. The differences between fresh water and saline water η are insignificant for the current analysis.

At an air-water boundary, for a specific radiation wavelength, the Fresnel reflection coefficient, ϱ_λ is a function of the reflection angle, Ω, and the complex refractive index of water, η, according to

$$
\begin{aligned}
a &= \left\{4\, m_r^2 m_i^2 + [m_r^2 - m_i^2 - \sin^2(\Omega)]^2\right\}^{1/2} \\
p^2 &= 1/2\, [-m_r^2 + m_i^2 + \sin^2(\Omega) + a] \\
q^2 &= 1/2\, [m_r^2 - m_i^2 + \sin^2(\Omega) + a]
\end{aligned}
$$

$$
\varrho_h\lambda = \frac{(q - \cos(\Omega))^2 + p^2}{(q + \cos(\Omega))^2 + p^2}
$$

$$
\varrho_v\lambda = \frac{[(m_r^2 - m_i^2)\cos(\Omega) - q]^2 + (2\, m_r\, m_i \cos(\Omega) - p)^2}{[(m_r^2 - m_i^2)\cos(\Omega) + q]^2 + (2\, m_r\, m_i \cos(\Omega) + p)^2}
$$

$$
\varrho_\lambda = 1/2\, [\varrho_{v\lambda} + \varrho_{h\lambda}] \qquad (4)
$$

where m_r is the real part of η; m_i is the imaginary part of η; $\varrho_{h\lambda}$ is the reflection coefficient for polarization perpendicular to the plane of incidence (horizontal polarization); $\varrho_{v\lambda}$ is the reflection coefficient for polarization parallel to the plane of incidence (vertical polarization); ϱ_λ is the reflection coefficient for unpolarized light; and the refractive index of air is assumed to be one (Stratton, 1941). Figure 4 shows the magnitude of the band-averaged, unpolarized, Fresnel reflection coefficient ϱ with relation to the reflection angle Ω. For angles near grazing, the surface is a reflector; whereas, for angles near normal incidence, the surface is an emitter.

The nonlinear form of the band-averaged ϱ, in terms of the wave-slope angle α, is shown in figure 5 for a sensor depression angle θ of 20 degrees. The magnitude of ϱ changes slightly for positive wave slopes and changes dramatically for negative wave slopes. This implies that (1) the sensor should not measure a significant change in radiance when it is looking at the front of a wave (assuming that the wave is traveling toward the sensor), and (2) the sensor should measure a large change in radiance when it is looking at the back side of a wave. The nonlinear ϱ-α relationship should cause troubles in determining the surface spectra, particularly if the sensor has a narrow field-of-view angle. Additional complications arise for cases of negative-angle slopes (back side of a wave), where there is the possibility of shadowing and double surface reflections.

Although theory clearly indicates considerable difficulties with using shape from reflection, a set of field measurements provided enough tantalizing information to continue pursuing the effort. In 1991, the Everest Interscience sensors were being used to monitor the sea-surface temperature to support a study of radar detection of low-altitude targets. These IR sensors were positioned 22 m above the ocean surface. Unfortunately, the sensor fov was restricted to looking in the surf zone, where breaking waves, sea foam, and other contaminants were present; however, with a slight

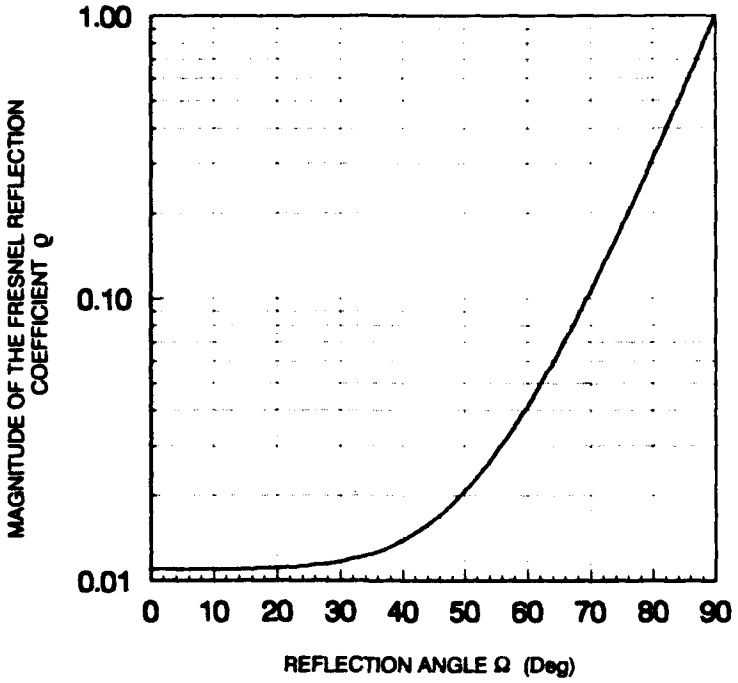

Figure 4. The band average Fresnel reflection coefficient for unpolarized light at an air-sea interface in relation to the reflection angle Ω.

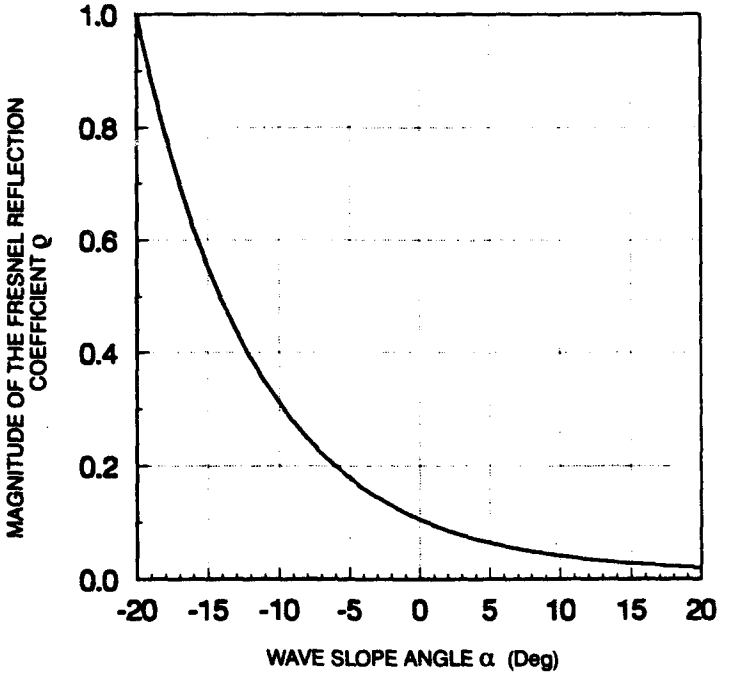

Figure 5. The band average Fresnel reflection coefficient for unpolarized light at an air-sea interface in relation to the wave slope angle α. The sensor depression angle θ is 20 degrees.

modification to the existing sensor system, a usable IR picture of the surf zone was made. Figure 6 shows a trend-removed time history of the IR signature in terms of temperature. The wavelike nature of the surf zone is clearly represented by the temperature fluctuations. First impressions of the data seem to indicate that changes in temperature amplitude could be related to the wave height; for example, figure 6 seems to indicate a large wave followed by three (or four) smaller waves, followed by three moderate waves, followed by a small wave, which is followed by three larger waves. This pattern of large and small waves could not be easily verified by a separate measurement. At the time, however, the wave structure in the surf zone was observed visually, and the height observations generally agree with the measured data; that is, larger waves appeared to yield larger temperature changes. A visual observation of the swell indicated a wave period of about 15 seconds. The periodicity is evident from the measured temperature data.

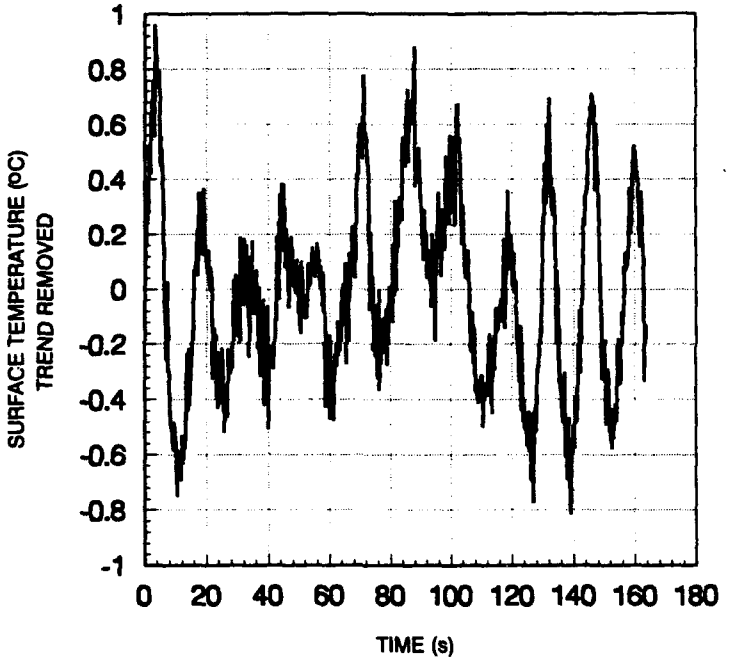

Figure 6. An IR signature of waves in the surf zone.

It is not possible to link the surf zone measurements directly to theory because of the surface contaminants (foam, sea weed, etc.) and their unknown effect on the radiance (temperature); however, the results were enticing enough to warrant testing the system under laboratory conditions. Funding was made available in January 1992, and a series of wave-tank measurements were made.

WAVE-TANK MEASUREMENTS

EQUIPMENT CONFIGURATION

Figure 7 illustrates the equipment set up at the Wind-Wave Channel facility at the Scripps Institution of Oceanography (SIO), San Diego, California. Interior dimensions of the tank are 44.5-m long, 2.39-m wide, and 2.44-m deep with a maximum water depth of 2 m. The wave generator is an electro-hydraulic, servo-controlled paddle that can create a maximum wave height of 60 cm. A tapered beach at the far end of the tank attenuates reflections, and the glass-walled tank can be enclosed on the top to allow blower-generated wind velocities up to 16 m/s over the water surface.

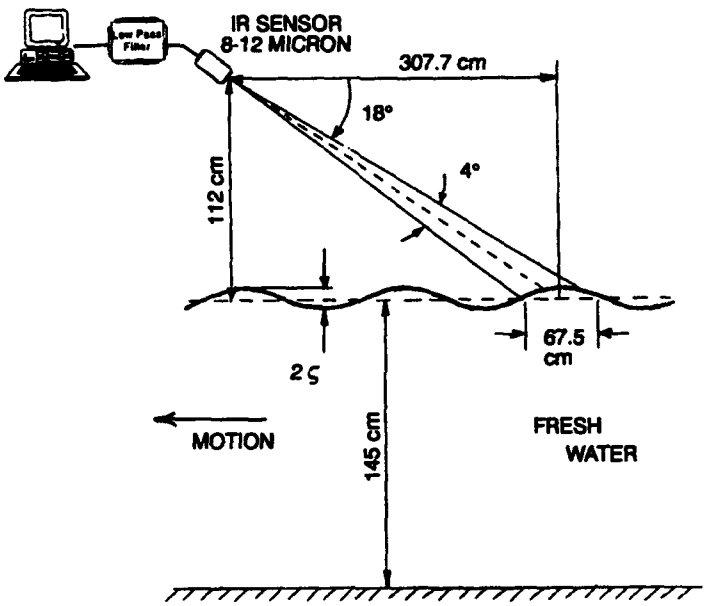

Figure 7. The equipment as set up at the SIO Wind-Wave Channel facility in San Diego, CA. The IR sensor was 112 cm above the still, fresh water surface and tilted downward at an angle of 20 degrees. A wave staff was positioned at the still-surface, beam-center, specular reflection point.

Wind effects on the surface were not examined. Only paddle generated waves were measured. The tank was filled to a depth of 145 cm with fresh water. There may have been some contamination of the surface because it was not skimmed before, or during, the 3 days of measurements (2–4 June, 1992); however, it was felt that if the technique did not work with a fairly clean facility there would be no chance of it working in the field.

SIO provided the wave staffs with their associated oscillator and buffer amplifier circuits. The signal output was calibrated for wave height by using a graduated scale attached to the wave staff. While the staff was moved up and down in still water, the height above the surface and the signal

voltage were recorded. Figure 8 shows a calibration curve that was recorded on 3 June 1992 at 1230 PDT; the circles represent the measured points. The ordinate is the surface function or surface height ζ (in cm), which is measured relative to the still surface. A linear fit to this calibration curve yields a correlation coefficient of 0.999969. Most of the other calibrations made during the measurement period were also nearly linear. Although not directly measured, schematics of the wave staff electronics indicate that the high frequency cutoff of the output amplifier circuit is about 6 Hz. The rolloff of the response is estimated to be about 6 dB per octave.

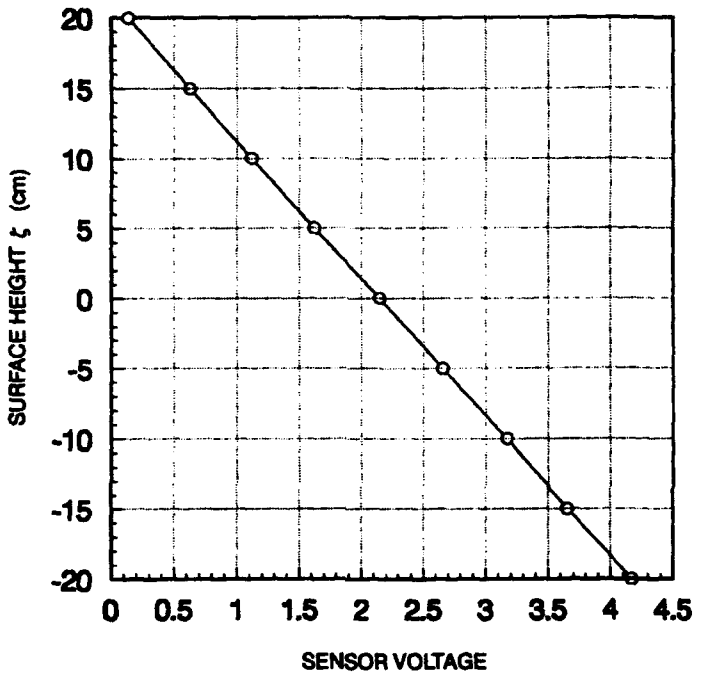

Figure 8. A typical wave staff voltage-versus-surface height calibration.

Prior to installation at the SIO facility, an Everest Interscience, Model 4000, IR sensor and its signal conditioning circuitry were tested to determine the frequency response. A camera shutter, with an aperture of 1.4 cm, was placed between the IR sensor and a heated pot of water. The conditioned output voltage was recorded prior to, during, and after opening the camera shutter. Figure 9 shows a typical response curve. The rise time of the leading edge is about 12.5 ms (approximately 2 ms is due to the shutter); the effective time constant of the system is about 33 ms.

It was decided to set the analysis cutoff frequency at 10 Hz, a frequency greater than the high frequency cutoff of the wave staffs and about one-third of the IR transducer high frequency cutoff. Two independent 11-pole Chebyschev, low-pass filters were constructed using Datel (Model FLJ-D5LA1 and FLJ-D6LA1) active filters. The voltage-versus-frequency response of the anti-aliasing filters is shown in figure 10. At a frequency of 10 Hz, the voltage response is 2 dB down; at 15 Hz, the voltage response is greater than 30 dB down.

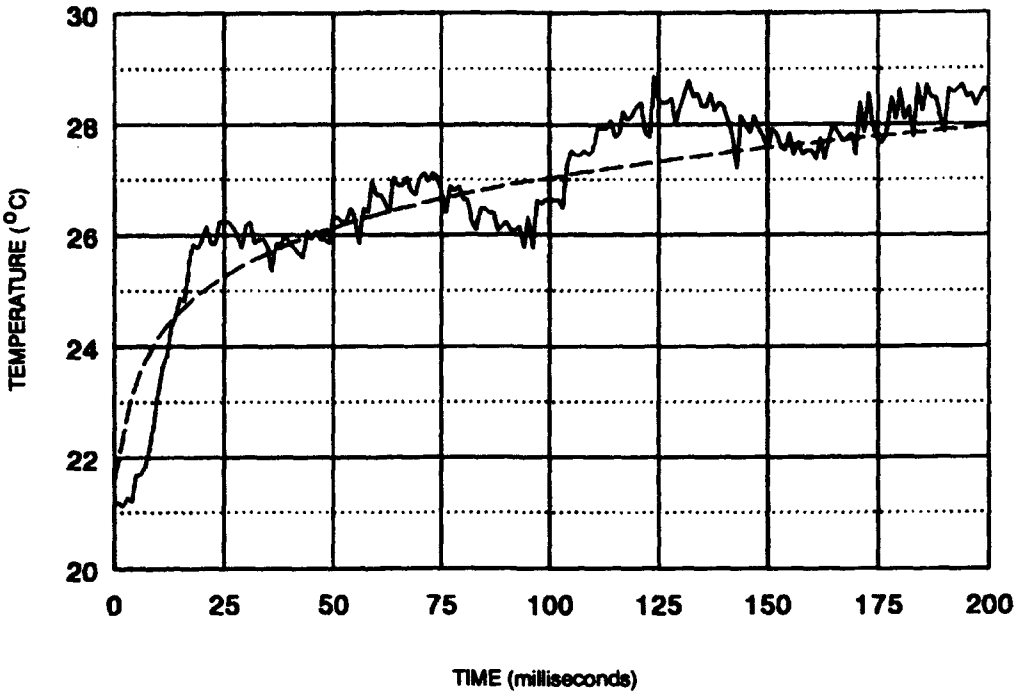

Figure 9. Step response of the IR sensor.

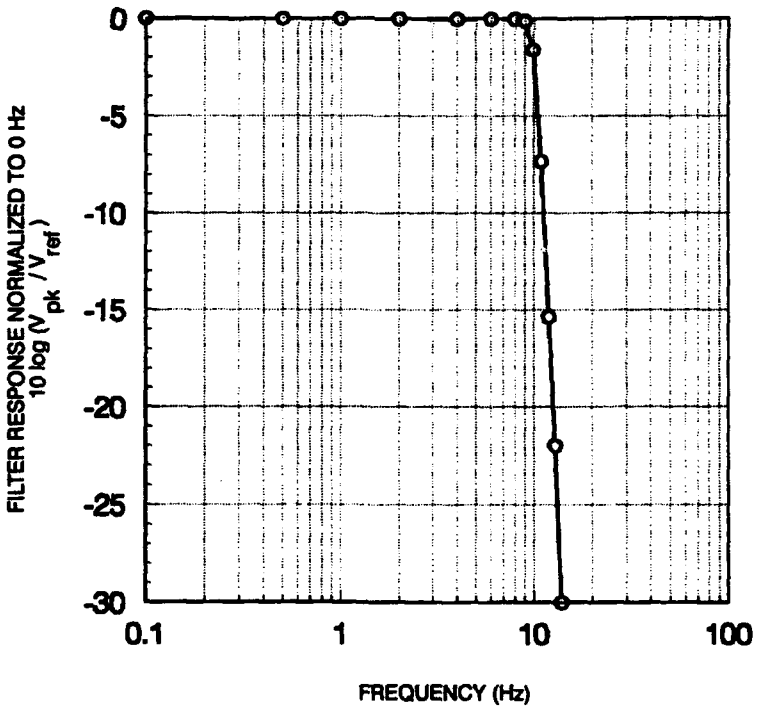

Figure 10. Normalized voltage response of the anti-aliasing filters.

An IR sensor head was positioned in the center of the Wind-Wave Channel at 112 cm above the still surface and approximately 10 m from the wave generating paddle. The depression angle θ of the sensor was set to 20 degrees by using an inclinometer. A resistive wire wave staff was positioned about 307.7 cm upstream near the edge of the channel at the still-surface beam-center specular reflection point of the sensor (figure 7). Later in the measurement period, a second wave staff was added 69.8 cm downstream from the first to determine the phase velocity of the waves.

Analog data from both the IR and the wave staff were digitized by a 12-bit analog-to-digital (A/D) converter that sampled the data at a 32-Hz rate. The A/D converter, a National Instruments, Model MIO-16, required a minimum of 25-μs delay between samples. Compared to the cycle interval of 31.25 ms, this delay is negligible and is ignored in the following analysis. All data were recorded under control of an IBM-compatible microcomputer. Typically, 11 sets of 1024 words per channel were stored per recording run.

Figure 11 shows the deep-water dispersion relation for free waves on still water. The angular frequency is

$$\omega^2 = g\,k + 72\,k^3 \tag{5}$$

where g is the acceleration of gravity (980 cm/s^2), and k is the angular wave number $2\pi/\lambda$ (Lamb, 1945). For gravity waves, wavelengths >> 1.7 cm, the phase velocity is found to be

$$C = g/\omega. \tag{6}$$

Figure 12 shows the cross–correlation between two wave staffs that were spatially separated by 69.8 cm. The wave staff records were made with a driving frequency of 1 Hz. The time to the first positive peak is 0.4687 s and the measured phase velocity C_o is 148.9 cm/s. A comparison to the calculated phase velocity C (156 cm/s) indicates good agreement between deep-water theory and measurements. Measured phase velocity at wave frequencies of 1.0, 0.8, and 0.6 Hz are shown as the three circles in figure 11.

The tests were conducted at the SIO facility over a three-day period, from 2–4 June 1992. Much of the first day was involved in equipment set up and preliminary testing. On the second day, testing was directed toward specular reflection measurements of a strong IR source (a portable electric heater) and ambient measurements of different driving frequencies with the tank covered in black plastic. The tank was covered to reduce stray reflections from the building interior. Testing on the last day was directed toward ambient measurements of different driving frequencies with the tank open to the "sky". The data from the 4 June measurement period is examined in the following section.

4 JUNE 1992 MEASUREMENTS

On 4 June 1992, a series of wave-tank measurements were made for wave frequencies of 1.0, 0.8, 0.6, and 0.4 Hz. Figure 13 shows the surface height ς and wave slope angle α for a 1-Hz wave of about 7-cm amplitude measured at 1205 PDT (1024 samples taken over a 32-second time interval). The abscissa, wave position, is the spatial coordinate (in cm) that would exist if the time coordinate were multiplied by the phase velocity C_o. A wave position of 0 is defined as the first sample in the data record. Multiple waves are observed; wave slopes vary from a maximum of about +10 to a minimum of about -10 degrees. Figure 14 expands the 20- to 30-m portion of the wave position for greater detail. Wave height and slope are shown to be reasonably well behaved.

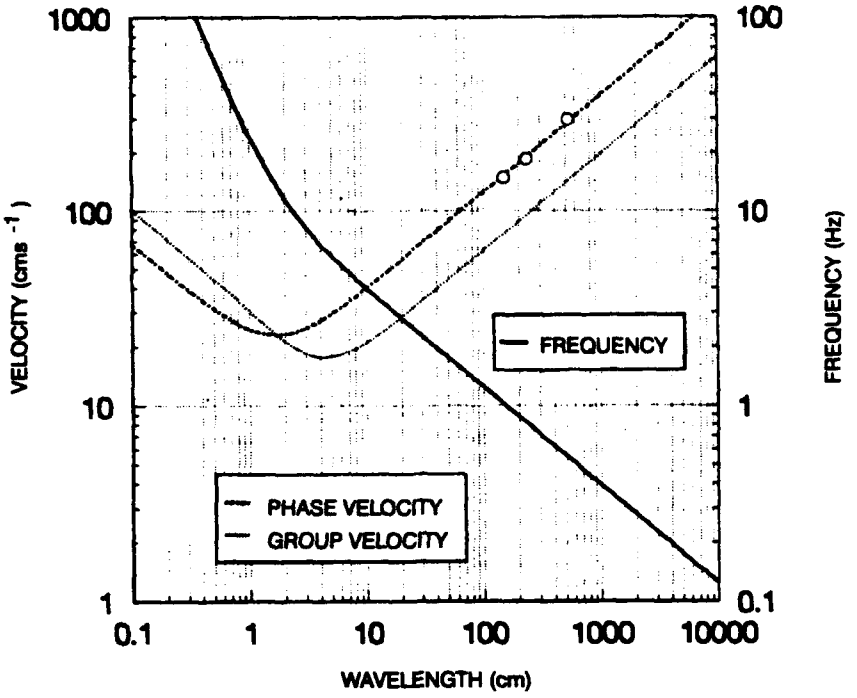

Figure 11. The dispersion relation for free waves on still water. The circles indicate measured phase velocities at frequencies of 1.0, 0.8, and 0.6 Hz.

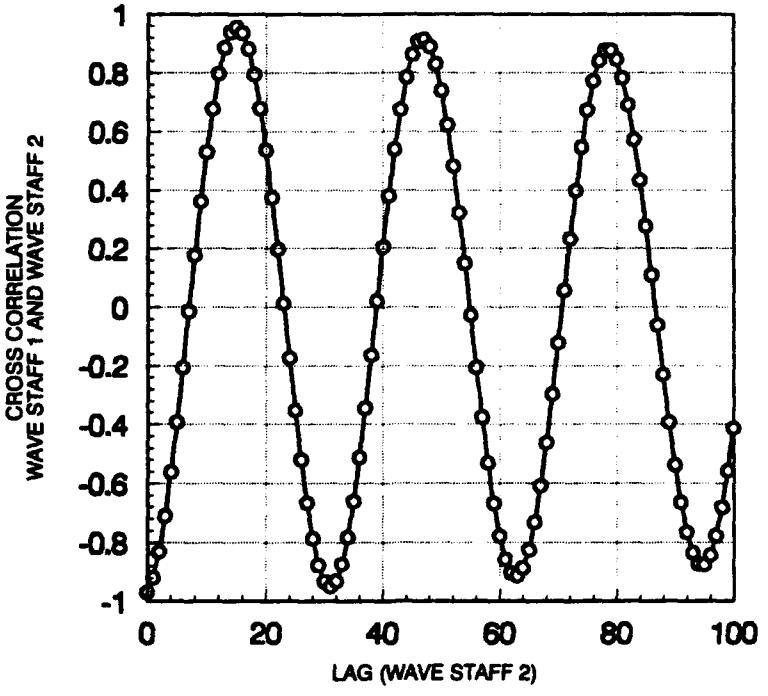

Figure 12. The cross correlation of two wave staffs separated by 69.8 cm. The measured phase velocity for a driving frequency of 1.0 Hz is 148.91 cm/s.

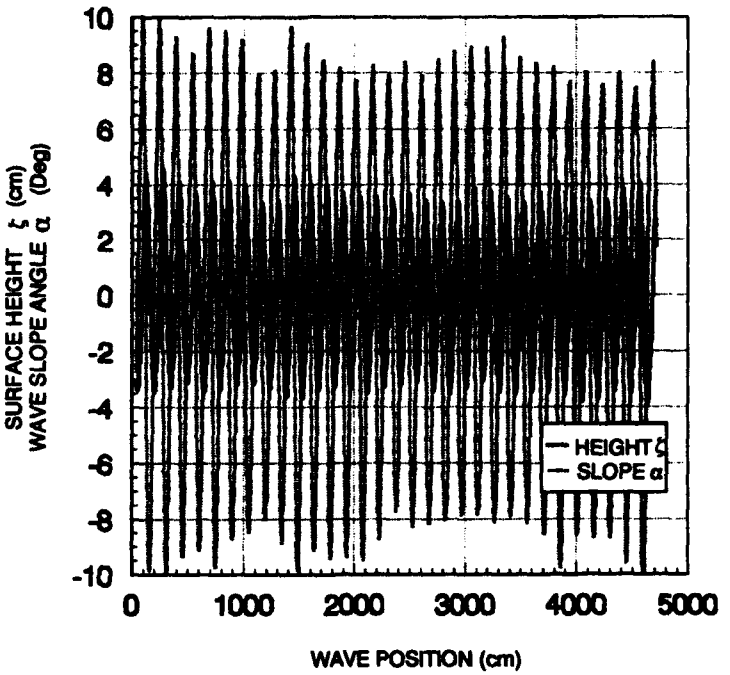

Figure 13. The surface height ζ and wave slope angle α for a 1-Hz wave of approximately 7-cm amplitude.

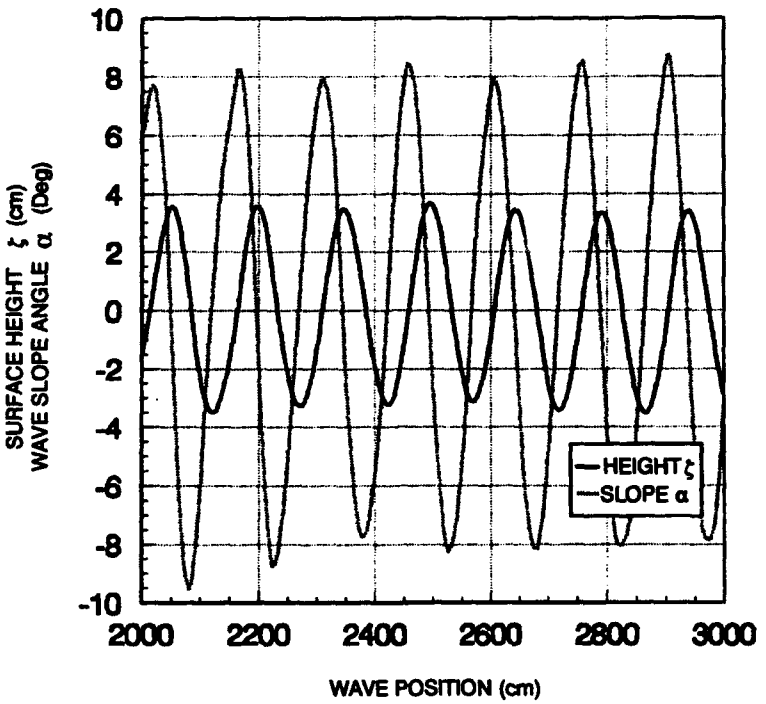

Figure 14. A detailed view of the 20- to 30-m portion of the wave position shown in the previous figure. Surface height and wave slope behave as expected.

Figure 15 expands the ζ data in even greater detail to illustrate the method of shape from refraction. Each circle on this figure represents a sample of the surface height as recorded by the wave staff. Assume that at some instant in time, say t_i, the wave staff measures the surface height at the wave position indicated by the arrow; surface heights to the left of the arrow were recorded prior to time t_i; whereas, surface heights to the right of the arrow were recorded after time t_i. At exactly time t_i, the IR sensor's fov (depicted as the shaded region in figure 15) falls on 11 surface facets: 5 facets to the left of the arrow position, and 6 facets to the right of the arrow position. For each of these 11 facets, the wave slope angle α is approximated as

$$\alpha = \tan^{-1}(\Delta\zeta/\Delta\chi) \tag{7}$$

where $\Delta\zeta$ is the height difference between consecutive samples, and $\Delta\chi$ is the position difference given by $C_o/32$. The depression angle θ is calculated by knowledge of the geometry between the center of the facet and the IR sensor (figure 7). The reflection angle Ω is related to θ and α as

$$\Omega = \pi/2 - \theta - \alpha \tag{8}$$

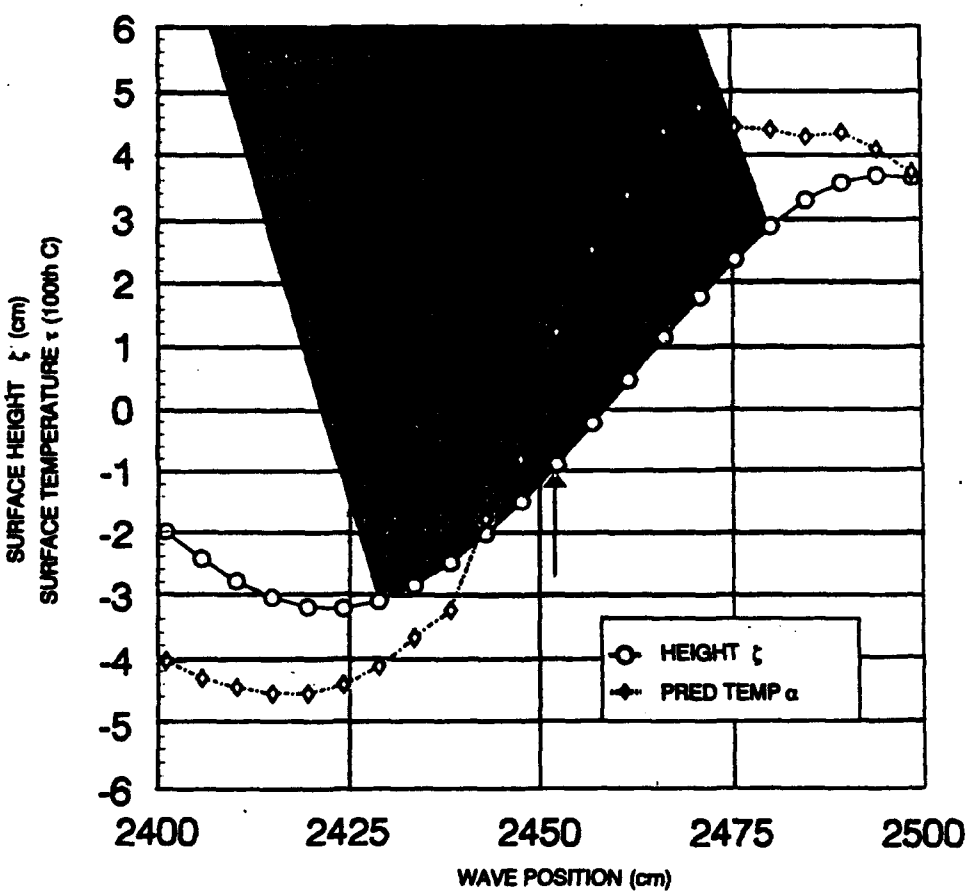

Figure 15. The 24- to 25-m portion of the wave position shown in figure 13. The shaded area represents the IR's sensor's field-of-view (figure 7) at the moment in time when the wave staff measured the wave height indicated by the arrow. The reflectance and emittance of the wave facets within the IR sensor's fov are summed to determine the temperature of the surface (shown by the chain line linking the diamond symbols).

The Fresnel reflection coefficient is readily found using the Ω-ϱ relation shown in figure 4. Through the T-L connection of figure 2, the bulk water temperature T_s and the "sky" ambient air temperature T_a that are recorded during the measurement period determine the band-averaged blackbody radiance from both the water surface and the air source. The values of T_s and T_a for this measurement are 20.9 and 21.6 Celsius, respectively. The band-averaged ambient emissivity is assumed to be one; therefore, the radiance as measured by the IR sensor at time t_i is approximated as

$$L_i = (1/\pi)\frac{1}{m+n}\sum_{j=i-n}^{i+m}[\beta_s(1-\varrho_j)+\beta_a\varrho_j] \tag{9}$$

where the indices m and n are chosen to satisfy the conditions of

$$112 - (307.7 + m\ C_o/32)\ \tan(18°) > \zeta_i + m, \quad \text{and}$$

$$112 - (307.7 + n\ C_o/32)\ \tan(22°) < \zeta_i + n, \tag{10}$$

These conditions simply require that the center of the wave facet be in the IR sensor field-of-view.

The radiance L_i is converted to a temperature T_i through the T-L connection of figure 2. The surface temperature fluctuation τ (in units of centidegree Celsius) is defined as

$$\tau_i = 100\ [T_i - (a_0 + a_1\ \chi_i)] \tag{11}$$

where χ_i is the wave position at time t_i, a_0 and a_1 are the coefficients of a linear least squares fit to the T-χ pairs calculated for the data record (typically 1024 pairs).

The surface temperature fluctuation calculated from knowledge of ζ, T_s, T_a, and C_o is shown in figure 15 as the chain curve connecting the diamond symbols. At time t_i, the surface temperature fluctuation is about +1.3 centidegree Celsius. The shape of the predicted τ curve is a distorted sinusoid; its negative peak occurs slightly before the negative peak of ζ, but its positive peak occurs considerably before the positive peak of ζ. The raggedness of the positive peak is attributed to the distortions in the ϱ-α relationship as α transitions from positive to negative angles (figure 5). Over the 20- to 30-m portion of the wave position shown in figure 16, the predicted τ curve illustrates the same characteristics as the detailed view.

Figure 17 compares the predicted to the measured surface temperature fluctuation. The measured curve (solid) appears to be offset in phase and also appears to be modulated; it has the characteristics of a beat frequency. The modulation is evident in the comparison of predicted to measured τ shown in figure 18. Although the magnitude of the predicted and measured τ agree reasonably well (which indicates that the assumptions used in shape from reflection theory are reasonable), the correlation of prediction and measurement are disappointing.

Figures 19–22 show the cross correlation between the measured and predicted τ for driving frequencies of 1.0, 0.8, 0.6, and 0.4 Hz, respectively. Each lag is 1/32 of a second. Table 1 lists the values of the correlation coefficient and the lag for the first three frequencies. The 0.4-Hz driven frequency experienced severe distortions in ζ that are probably related to poorly attenuated tank reflections and its correlation is low (figure 22). The correlation for the first three frequencies (there is considerable confidence in these measurements) show a marginal value of about 0.5. An indication of problems with the shape from reflection method is seen by the sign reversal of the

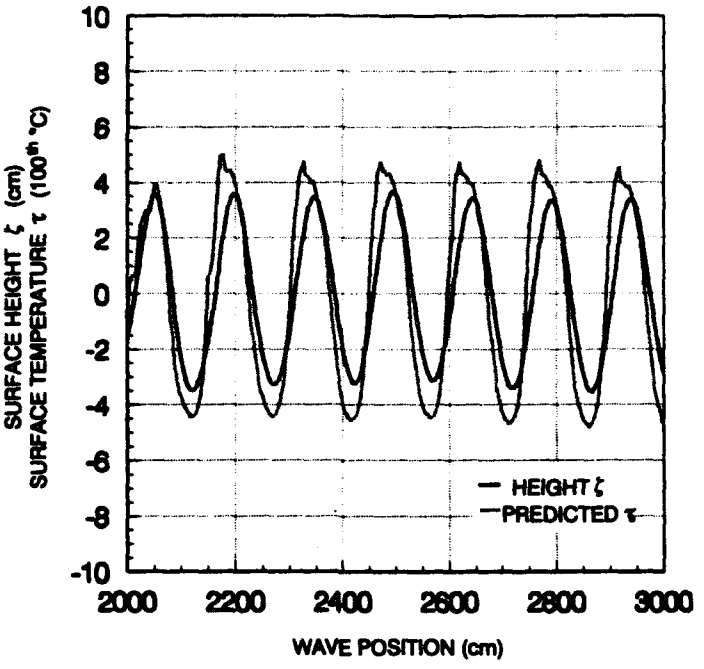

Figure 16. The surface height and the predicted surface temperature fluctuation (in centidegree Celsius) for the 20- to 30-m portion of the wave position shown in figure 13. The predicted surface temperature appears as a distorted sinusoid.

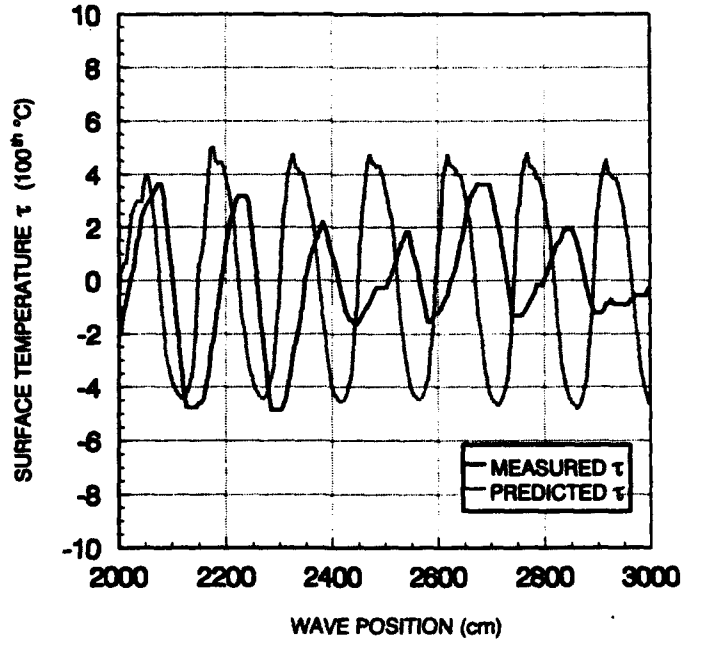

Figure 17. A comparison of the measured (solid line) and predicted surface temperature fluctuation. The measured temperature appears to be modulated; whereas, the predicted temperature is not modulated.

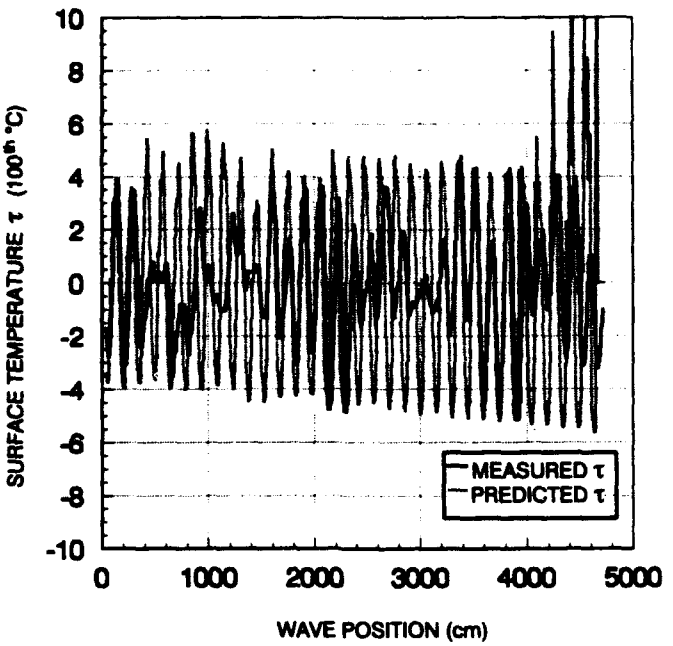

Figure 18. An expanded view of the predicted and measured surface temperature fluctuation. The beat frequency nature of the measured temperature is readily seen.

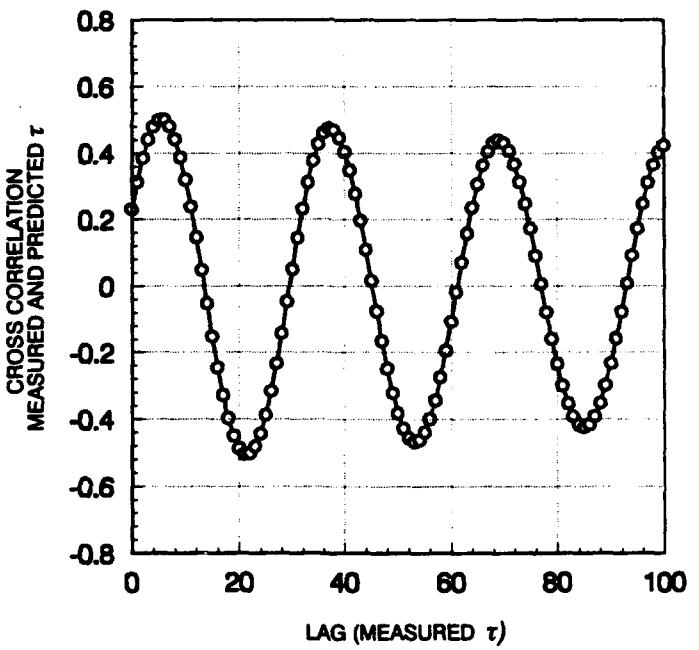

Figure 19. The cross correlation of the measured and predicted temperature fluctuation. Driving frequency is 1.0 Hz at an amplitude of about 7 cm.

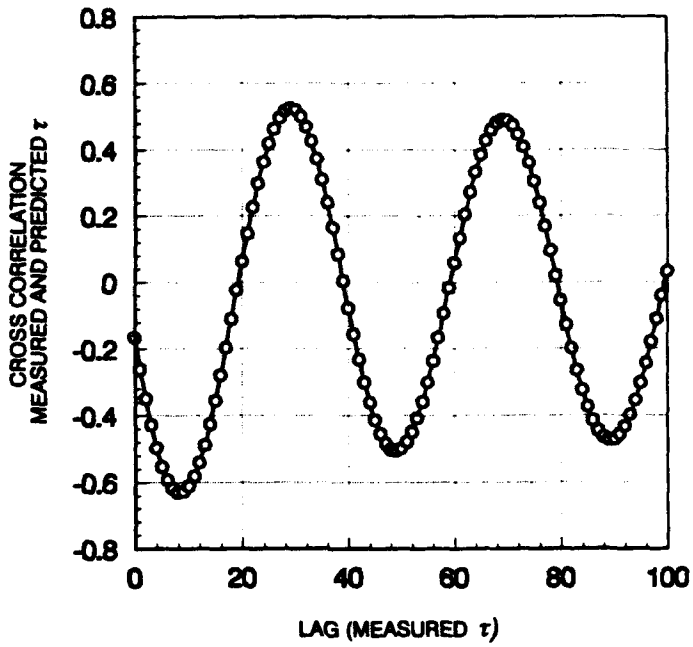

Figure 20. The cross correlation of the measured and predicted temperature fluctuation. Driving frequency is 0.8 Hz at an amplitude of about 10 cm.

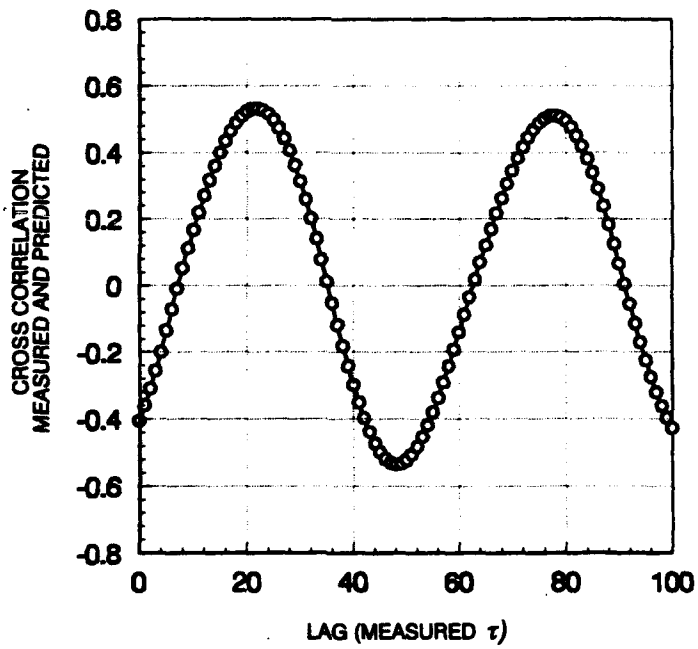

Figure 21. The cross correlation of the measured and predicted temperature fluctuation. Driving frequency is 0.6 Hz at an amplitude of about 10 cm.

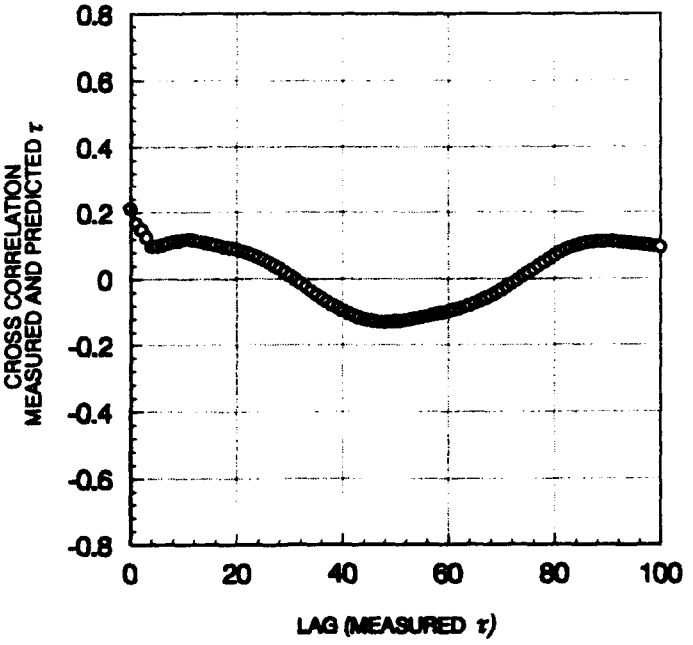

Figure 22. The cross correlation of the measured and predicted temperature fluctuation. Driving frequency is 0.4 Hz at an amplitude of about 8 cm.

correlation coefficient between driven frequencies of 1 and 0.6 Hz. From table 1, the first peak in correlation is about 0.5 for the 1- and 0.6-Hz frequencies; whereas, for the 0.8 Hz-frequency, the first wave peak in correlation is about –0.64.

Table 1. Correlation between measured and predicted temperature fluctuations.

Time (PDT)	Freq (Hz)	Wave Height ζ	Correl Coeff/ Lag	Correl Coeff/ Lag	Correl Coeff/ Lag	Correl Coeff/ Lag
1205	1.0	7	0.499/ 5	–0.504/ 21	0.474/ 37	–0.467/ 53
1239	0.8	10	–0.635/ 22	0.526/ 48	–0.506/ 78	0.491/ 69
1248	0.6	10	0.532/ 10	–0.535/ 48	0.511/ 78	--------/ --
1258	0.4	8	--------/ --	--------/ --	--------/ --	--------/ --

Figure 23 shows surface height ζ and wave slope α curves, and figure 24 provides measured and predicted τ curves for the first 16 seconds of data recorded with a driving frequency of 0.4 Hz. The nonsinusoidal shape of ζ is evident (cf figures 14 and 23). The measured phase velocity C_o of 297.8 cm/s does not compare to the predicted phase velocity C of 389.9 cm/s; a measurement error is suspected; however, the measured phase velocity was used to calculate the wave slopes. The slopes are strongly affected by the ζ distortions and have considerable impact on the calculation of ϱ and the predicted τ. Even though the correlation of measured and predicted τ is very poor (figure 22), the comparisons shown in figure 24 are qualitatively good. There are deviations between the two curves, but there are also periods of agreement. The magnitudes are in general agreement, and the trends appear visually related. In particular, the comparison in the interval from 10 to 14 seconds is remarkable. One can argue the fact that even random data align sometimes, but the overall sense of agreement of the measured to predicted τ was encouraging; however, the intent of shape from reflection is to relate the measured τ to ζ. The results of these comparisons are disappointing.

Figures 25–28 are the cross correlation between the measured τ and the measured ζ for wave frequencies of 1.0, 0.8, 0.6, and 0.4 Hz respectively. Table 2 lists the values of the correlation coefficient and the lag for the four frequencies. Even though the 0.4-Hz wave frequency experienced severe distortions in ζ (figure 23), the cross correlation coefficient is not substantially different from the coefficient for the other frequencies; however, the magnitude of the "average" correlation coefficient, about 0.6, is marginal. In addition, the sign change of the correlation coefficient between frequencies is disturbing.

Table 2. Correlation between measured temperature fluctuations and surface height.

Time (PDT)	Freq (Hz)	Wave Height ζ	Correl Coeff/ Lag	Correl Coeff/ Lag	Correl Coeff/ Lag
1205	1.0	7	0.575/ 4	–0.557/ 19	0.538/ 37
1239	0.8	10	–0.680/ 13	0.666/ 33	–0.642/ 53
1248	0.6	10	–0.741/ 3	–0.722/ 31	–0.688/ 58
1258	0.4	8	0.476/ --	–0.445/ 27	--------/ 69

Further evidence of the limitations of shape from reflection is shown in figures 29–32, which are the distributions of measured τ and measured ζ for wave frequencies of 1.0, 0.8, 0.6, and 0.4 Hz, respectively. These figures are derived from 10,240 samples (10 data recordings of 1024 samples) of each frequency. The height distribution is about what one would expect for a sinusoidal function. Its classic cusp shape is expected to peak near maximum and minimum values of ζ. The distribution of measured surface temperature τ has no relationship to the ζ distribution. If anything, the τ distributions shown in figures 29–32 resemble a distribution of a random process, not a sinusoidal process.

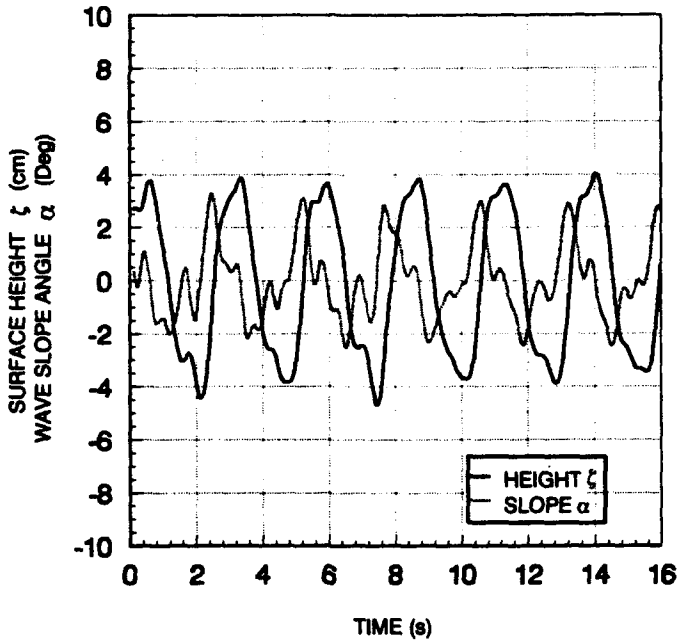

Figure 23. Surface height ζ and wave-slope angle α for waves of 8 cm amplitude at a driving frequency of 0.4 Hz. The height and slope are not sinusoidal.

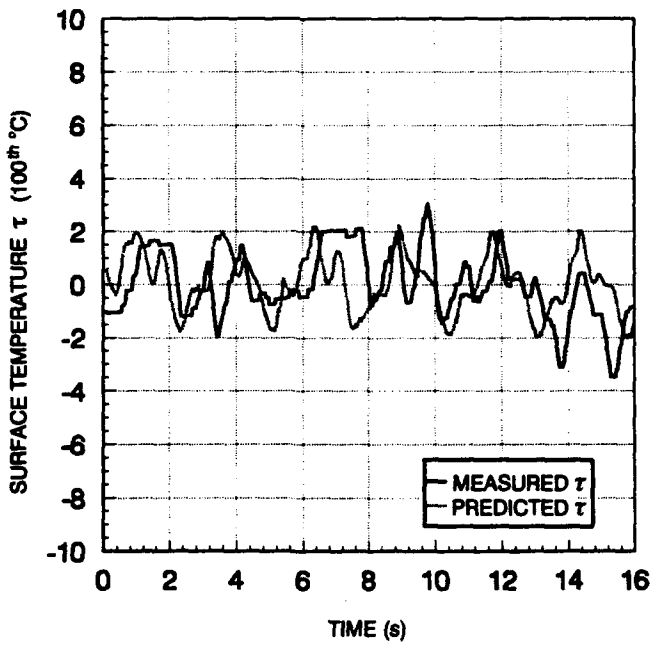

Figure 24. Measured and predicted surface temperature fluctuation for waves of 8 cm amplitude at a driving frequency of 0.4 Hz.

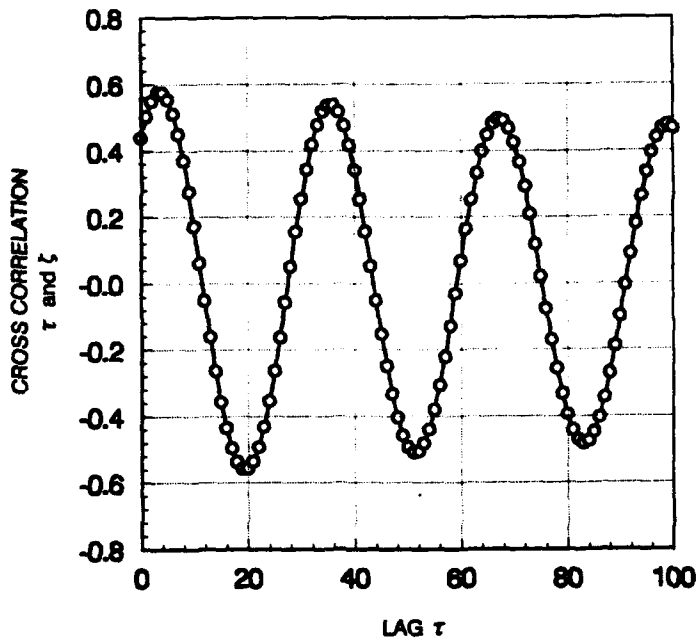

Figure 25. The cross correlation of the measured temperature fluctuation and the measured surface height. Driving frequency is 1.0 Hz at an amplitude of about 7 cm.

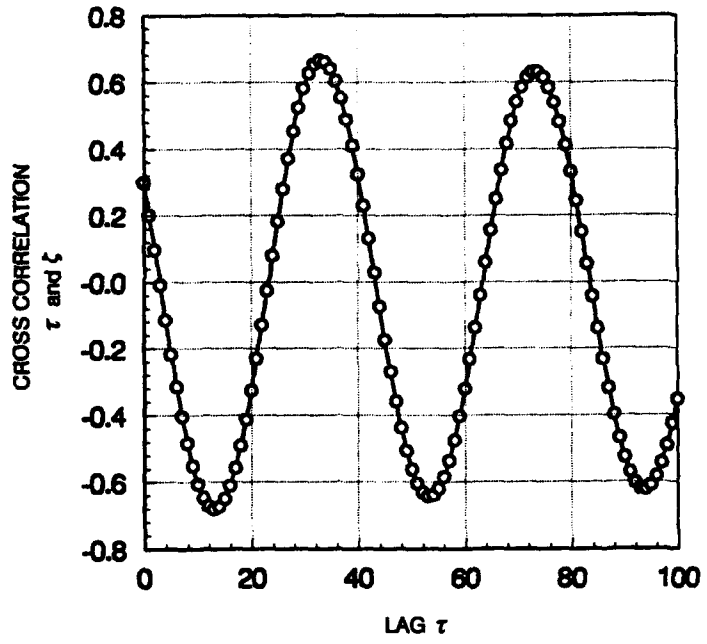

Figure 26. The cross correlation of the measured temperature fluctuation and the measured surface height. Driving frequency is 0.8 Hz at an amplitude of about 10 cm.

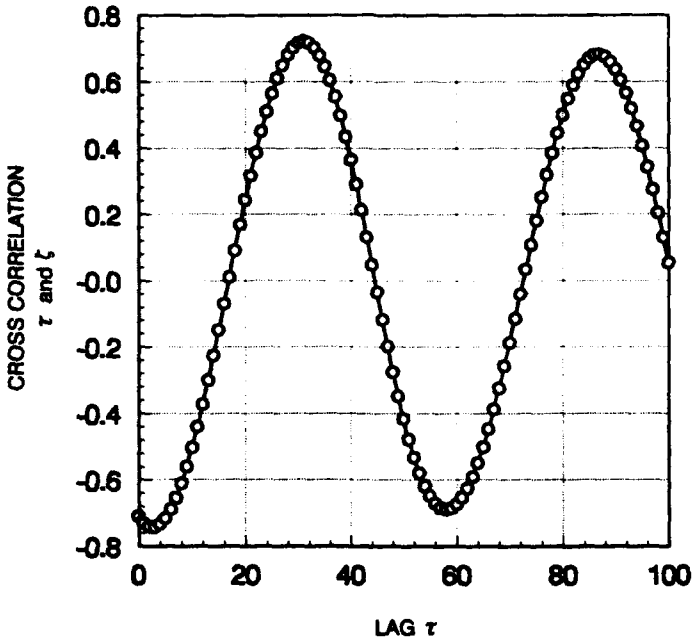

Figure 27. The cross correlation of the measured temperature fluctuation and the measured surface height. Driving frequency is 0.6 Hz at an amplitude of about 10 cm.

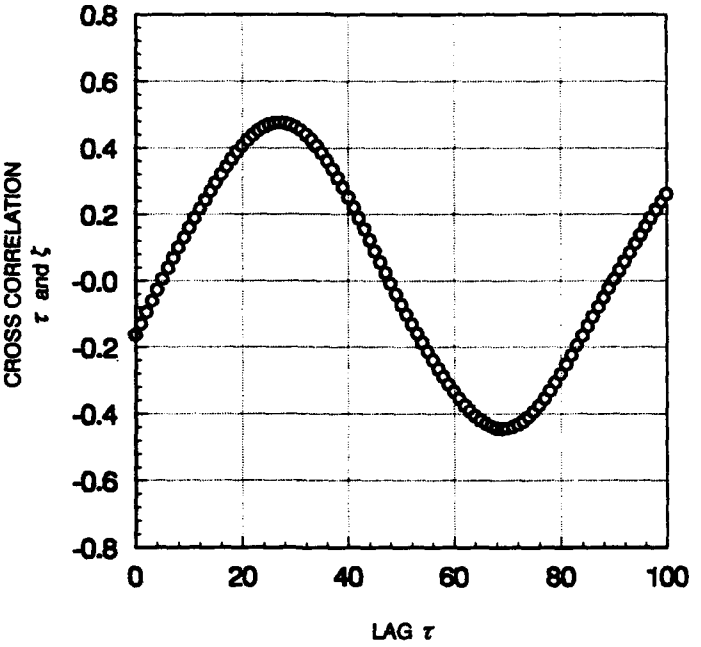

Figure 28. The cross correlation of the measured temperature fluctuation and the measured surface height. Driving frequency is 0.4 Hz at an amplitude of about 8 cm.

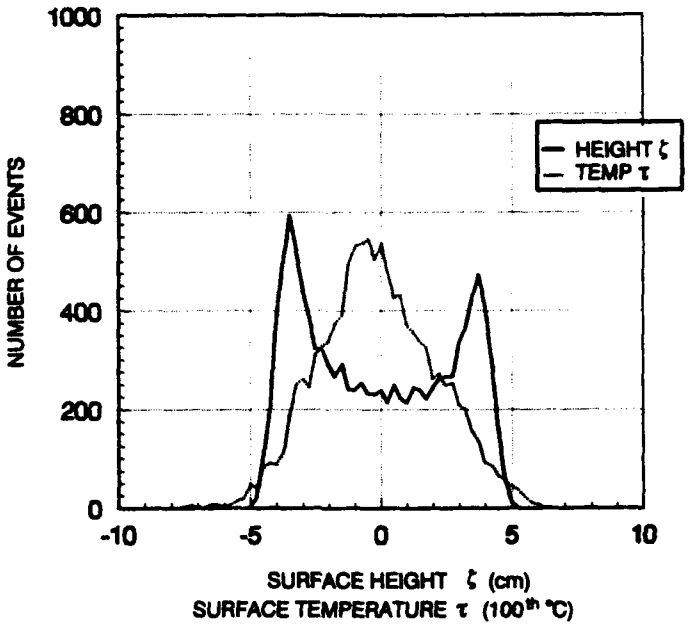

Figure 29. The distributions of measured surface height ζ and measured temperature fluctuation τ. Driving frequency is 1.0 Hz at an amplitude of about 7 cm.

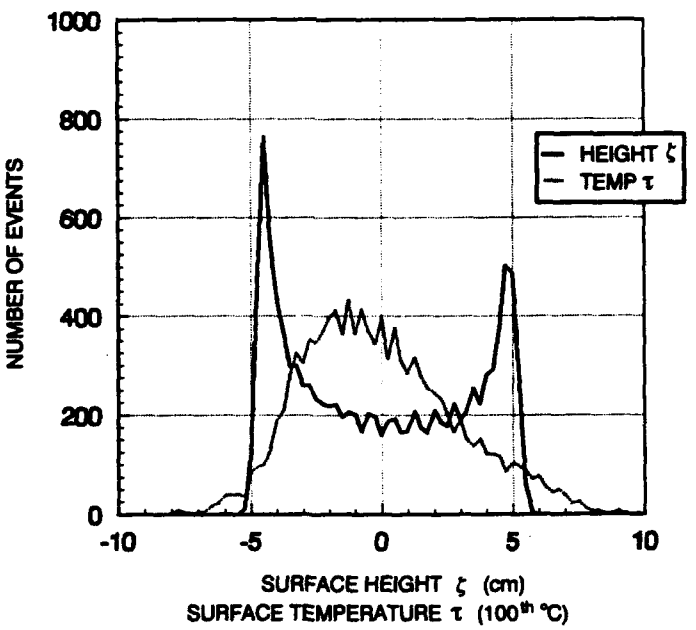

Figure 30. The distributions of measured surface height ζ and measured temperature fluctuation τ. Driving frequency is 0.8 Hz at an amplitude of about 10 cm.

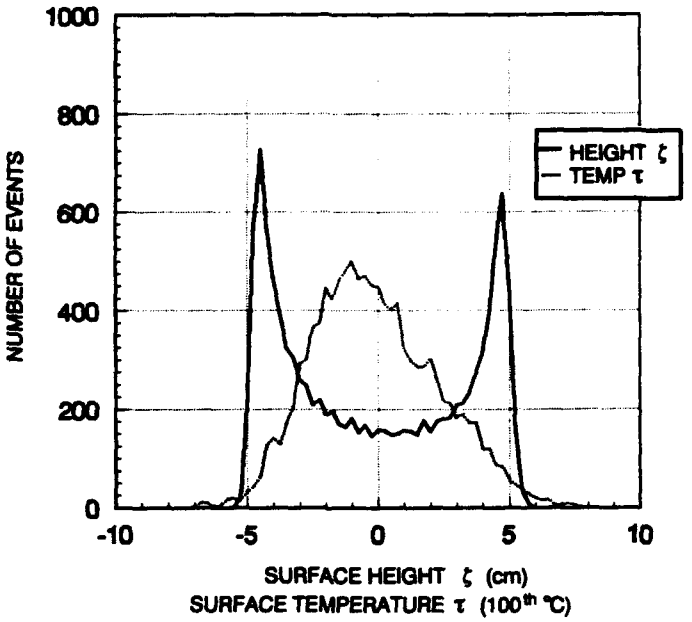

Figure 31. The distributions of measured surface height ζ and measured temperature fluctuation τ. Driving frequency is 0.6 Hz at an amplitude of about 10 cm.

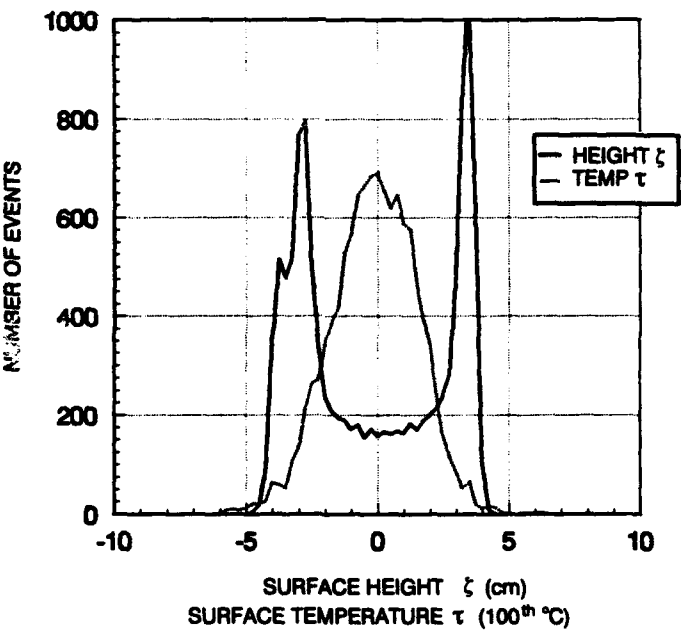

Figure 32. The distributions of measured surface height ζ and measured temperature fluctuation τ. Driving frequency is 0.4 Hz at an amplitude of about 8 cm.

On 4 June 1992, measurements were made with the tank open to the sky. On the previous day, measurements were made with the tank covered in black plastic to minimize angular variations in the sky luminance function. However, irrespective of whether or not the tank was covered, there is no significant difference in the comparisons of measured to predicted data; the 4 June measurements are typical of what was seen with the tank covered. In the following paragraphs, measurements from both days are used to examine the surface height variance.

SURFACE VARIANCE

The variance of the surface height is a useful and readily observable statistic. In its simplest form, the variance is

$$v^2 = 1/(N - 1)\sum [x - < x >]^2 \qquad (12)$$

where N is the number of x variables, and <x> is the average or expected value of x. In a more complicated form, the power spectrum is the frequency distribution of variance.

Figure 33 compares the variance of the measured surface temperature τ to the variance of the measured surface function ζ for four driving frequencies. The solid (filled) symbols correspond to data taken on 3 June 1992 (tank covered); the open (not filled) symbols correspond to data taken on 4 June 1992. Each symbol (solid or open) is the variance of 1024 samples (N = 1024). It is obvious that the surface temperature variance is not consistently related to the variance of the height.

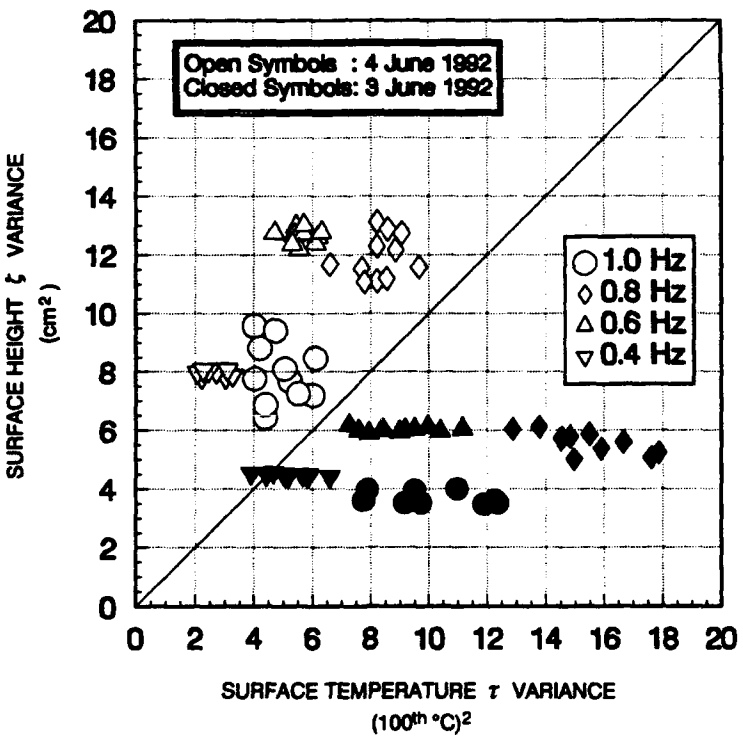

Figure 33. Comparison of measured surface temperature variance and measured surface height variance. The open symbols represent data that were taken with the tank open to the sky; the filled symbols represent data that were taken with the tank covered.

CONCLUSIONS

Shape from reflection is not a viable technique to determine the simplest statistics required to describe the ocean surface. Although the technique appears to have merit (e.g., figures 6 and 24), the qualitative is not supported by the quantitative. Correlations of measured and predicted temperature fluctuations (figures 19–22 and table 1) are poor; the average correlation coefficient is about 0.5. Correlations of measured temperature fluctuations and surface height (figures 25–28 and table 2) are also poor, averaging about 0.6. These correlations are for near laboratory conditions; it is expected that the correlations in actual field conditions would not be any better.

The death knell of shape from reflection is provided by figures 29–32. The comparisons of the distributions for the measured temperature fluctuation and the measured surface height are very poor. The surface height is the classic sinusoidal cusp shape; whereas, the temperature fluctuation appears to be more of a random variable distribution. Clearly, if the distributions do not match, it is highly unlikely that there is any meaningful relationship between the surface temperature fluctuation and the surface height.

An investigation of a promising technique to routinely measure ocean surface roughness characteristics has conclusively demonstrated that shape from reflection is not appropriate for fleet operations.

REFERENCES

Hale, G. M., and Querry, M. R. 1973. "Optical Constants of Water in the 200-nm to 200-μm Wavelength Region," *Applied Optics*, vol. 12, no. 3, March , pp. 555–563.

Jahne, B., Waas, S., and Klinke, J. 1992. "A Critical Theoretical Review of Optical Techniques for Short Ocean Wave Measurements," International Symposium on *Optical Applied Science and Engineering*, SPIE Proc. Vol. 1749, *Optics of the Air-Sea Interface*: Theory and Measurements. July 19–24, San Diego, CA.

Lamb, H. 1945. *Hydrodynamics*, 6th ed., Dover Publications, New York, NY.

Querry, M. R., Holland, W. E., Waring, R. C., Earls, L. M., and Querry, M. D. 1977. "Relative Reflectance and Complex Refractive Index in the Infrared for Saline Environmental Waters," JGR, vol. 82, no. 9, March 20, pp. 1425–1433.

Stilwell, D., Jr. 1969. "Directional Energy Spectra of the Sea from Photographs," JGR, vol. 74, no. 8, April 15, pp. 1974–1986.

Stratton, J. A. 1941. *Electromagnetic Theory*, McGraw-Hill, New York, NY.

REPORT DOCUMENTATION PAGE

Form Approved
OMB No. 0704-0188

1. AGENCY USE ONLY *(Leave blank)*	2. REPORT DATE	3. REPORT TYPE AND DATES COVERED
	May 1993	Final: May 1993

4. TITLE AND SUBTITLE
OCEAN SURFACE ROUGHNESS FROM INFRARED MEASUREMENTS: A FAILURE OF SHAPE FROM REFLECTION

5. FUNDING NUMBERS
ACC: DN302214
PE: 0602435N
PN: R035E81

6. AUTHOR(S)
K. D. Anderson

7. PERFORMING ORGANIZATION NAME(S) AND ADDRESS(ES)
Naval Command, Control and Ocean Surveillance Center (NCCOSC)
RDT&E Division
San Diego, CA 92152–5001

8. PERFORMING ORGANIZATION REPORT NUMBER
TR 1609

9. SPONSORING/MONITORING AGENCY NAME(S) AND ADDRESS(ES)
Naval Command, Control and Ocean Surveillance Center (NCCOSC)
RDT&E Division
San Diego, CA 92152–5001

10. SPONSORING/MONITORING AGENCY REPORT NUMBER

11. SUPPLEMENTARY NOTES

12a. DISTRIBUTION/AVAILABILITY STATEMENT
Approved for public release; distribution is unlimited.

12b. DISTRIBUTION CODE

13. ABSTRACT *(Maximum 200 words)*

The objective of this effort is to test the practicality of an instrument that uses the reflection coefficient modulated radiance (shape from reflection) to measure the roughness of the sea surface. Conceptually, this instrument would be used aboard ship to remotely sense the ocean wave spectrum of the sea surface; ideally, the ocean wave spectrum covered by this instrument would range from very long wavelengths, on the order of decameters, to very short wavelengths, on the order of centimeters. A series of wave tank measurements made at the Scripps Institution of Oceanography (SIO), San Diego, CA, clearly show that the technique is impractical. The technical difficulties are associated with the failure of several necessary assumptions of shape from reflection. The first assumption is that the "sky" illumination source is nearly isotropic; in practice, this assumption is not valid. The second assumption is that the nonlinear relationship between the reflection coefficient and wave slope is not a fundamental limiting factor; in practice, the sensitivity of the reflection coefficient to incidence angle appears to be a limiting factor. The technique of measuring the ocean wave spectrum by shape from reflection is not viable and should not be pursued.

14. SUBJECT TERMS
electromagnetic
propagation
atmosphere

15. NUMBER OF PAGES
37

16. PRICE CODE

17. SECURITY CLASSIFICATION OF REPORT	18. SECURITY CLASSIFICATION OF THIS PAGE	19. SECURITY CLASSIFICATION OF ABSTRACT	20. LIMITATION OF ABSTRACT
UNCLASSIFIED	UNCLASSIFIED	UNCLASSIFIED	SAME AS REPORT

21a. NAME OF RESPONSIBLE INDIVIDUAL	21b. TELEPHONE *(include Area Code)*	21c. OFFICE SYMBOL
K. D. Anderson	(619) 553–1420	Code 543

INITIAL DISTRIBUTION

Code 0012	Patent Counsel	(1)
Code 0141	A. Gordon	(1)
Code 0142	K. Campbell	(1)
Code 02712	Archive/Stock	(6)
Code 0274B	Library	(2)
Code 54	J. H. Richter	(1)
Code 543	K. D. Anderson	(25)

Defense Technical Information Center
Alexandria, VA 22304-6145 (4)

NCCOSC Washington Liaison Office
Washington, DC 20363-5100

Center for Naval Analyses
Alexandria, VA 22302-0268

Navy Acquisition, Research and Development
Information Center (NARDIC)
Washington, DC 20360-5000

GIDEP Operations Center
Corona, CA 91718-8000

NCCOSC Division Detachment
Warminster, PA 18974-5000

University of California, San Diego
Scripps Institute of Oceanography
La Jolla, CA 92093